Chapter 6

INTRODUCTION

Autonomous underwater vehicles (AUVs) have received recent attention as a means of performing underwater missions that are unattainable by a human operator due to accessibility constraints, hazardous conditions or operational cost. They have become useful tools for many applications, such as deep water exploration and surveying, ocean sensing, maintenance of offshore oil installations and wind turbines, spill inspection and military operations (Griffiths, 2002; Roper et al., 2011). Because they function in such extreme environments, AUVs necessitate state-of-the-art capabilities. Their propulsion mechanisms must be highly efficient in order to reach long ranges with the limited available power. They are often imposed strict noise constraints to prevent being detected or perturbing their surroundings and require rapid maneuverability to operate in reduced spaces and avoid impact from foreign objects.

The vast majority of existing aquatic vehicles employs traditional screw propellers, which have been optimized for decades to reach propulsive efficiencies up to 70% (Carlton, 2007; Fish, 2013). The propulsion mechanism is currently responsible, however, for the majority of the radiated noise, with much of this noise being caused by cavitation (Carlton, 2007; Fish, 2013). The past decade has seen a rise in the development of bio-inspired propellers, that constitute great candidates for AUV propulsion. Due to their lower velocities, bio-inspired propellers do not generally present cavitation and naturally radiate much lower levels of noise, with their signature being, additionally, harder to identify (Carlton, 2007; Fish, 2013). The propulsive efficiency of swimming animals has been reported to reach values of up to 90% (Fish, 1998; Rohr and Fish, 2004). While existing fish-inspired propellers are far from that value (Techet, 2008; Triantafyllou et al., 2000; Wen et al., 2013) they have the potential to approach it if optimally designed and may result in higher efficiencies than those attainable by screw propellers.

From a biological standpoint, the swimming locomotion of fish is typically classified into two main types according to the body part employed to generate the force: body and caudal fin (BCF) propulsion and median and paired fin (MPF) propulsion (Sfakiotakis et al., 1999). BCF propulsion functions by generating a lateral wave that

travels backwards through the animal's body and caudal fin and can be subdivided into separate modes according to the portion of the body that sees a significant wave amplitude. The highest propulsive efficiencies are achieved by thunniform swimmers, that possess a fairly rigid body and present significant lateral motions at the caudal fin and peduncle only. Fish that are more flexible or utilize MPF propulsion are less efficient cruisers but greatly surpass thunniform swimmers in maneuverability Webb (1984); Weihs (1973).

From an engineering perspective the underwater propulsion mechanisms of animals can be classified according to the fluid forces they are based on: drag, lift or acceleration reaction (Fish, 2013; Sfakiotakis et al., 1999). Drag-based propulsion generally involves two strokes. In the power stroke the appendage is bluff and generates a large pressure drag, while in the recovery stroke it streamlines to return to its initial position with minimum forces. Drag forces are generated by paddling animals and some types of MPF swimmers and can be utilized for precise maneuvering. Acceleration reaction forces correspond to the added mass effect and are present in jetting propulsion and undulatory swimming. Lift forces are generated by the relatively stiff caudal fins of thunniform swimmers and cetaceans and result in the highest propulsive efficiency of the three types.

Due to this high cruising efficiency, lift-based caudal-fin propulsion is a particularly promising line of research. As has been hinted in the previous paragraphs, there is, however, a trade-off between long-range propulsive efficiency and maneuverability (Fish, 2002). AUV bodies are typically comprised of rigid cylindrical vessels, because these are resistant to compression at high pressures and compatible with modular construction (Roper et al., 2011). A rigid AUV that is propelled by a lift-based flapping propeller attached to its rear end will possess limited maneuverability if no additional surfaces or mechanisms are present. To overcome this limitation, multiple studies have proposed the use of flexible bodies (Marchese et al., 2014; Su et al., 2014). The focus of this work, however, is the improvement of the maneuverability of AUVs that must maintain a rigid body due to payload limitations. The maneuvering performance of a caudal-fin propeller that can perform large rotations in all three degrees of freedom is investigated, with the prospect that these complex 3D motions will allow to obtain a highly efficient and highly maneuverable single-fin flapping propeller for AUV use.

6.1 Objectives

A fin that is capable of rotation in all three degrees of freedom can follow an infinite number of different trajectories in its motion. The aim of this study is to obtain the best trajectory that generates a specified desired maneuvering force. The number of possible motions can be reduced by considering a family of trajectories that are defined by a finite number of parameters. In this work ten different degrees of freedom will be considered. Because this number is quite large, sweeping over all combinations of parameters is not viable. Employing an optimization algorithm largely reduces the number of tests that need to be performed in order to find an optimum. This optimization has been performed making use of the experimental setup developed by Martin and Gharib (2018). The optimal trajectories obtained for fins of varying properties will be analyzed in the following chapters. Part II of this thesis is organized as follows

- The remainder of Chapter 6 is dedicated to describing the optimization process and experimental setup
- Chapter 7 investigates the optimal trajectory for fins of high aspect ratio
- Chapter 8 examines the effect of adding flexibility to the fin on the optimal trajectory
- Chapter 9 concludes Part II and highlights the most promising directions for future research

6.2 Optimization procedure

Several existing studies have explored the optimization of propeller properties and motion to obtain maximum propulsive force, efficiency, energy, velocity or lift force both in bio-inspired and screw propellers, as well as in flapping wings (Berman and Wang, 2007; Clark et al., 2012; De Margerie et al., 2007; Kato and Liu, 2003; Martin and Gharib, 2018; Milano and Gharib, 2005; Rakotomamonjy et al., 2007; Tuncer and Kaya, 2005). Due to the ease of interfacing, most of these studies were performed computationally, where the evaluation of fitness in each step of the optimization algorithm was assessed through numerical methods. Because fully resolved simulations are expensive for such a large number of evaluations, these studies are limited to optimizing simplified models and a small number of parameters at low Reynolds numbers. Experimental assessment of the fitness of each optimization step eliminates these limitations, albeit adding a level of complexity

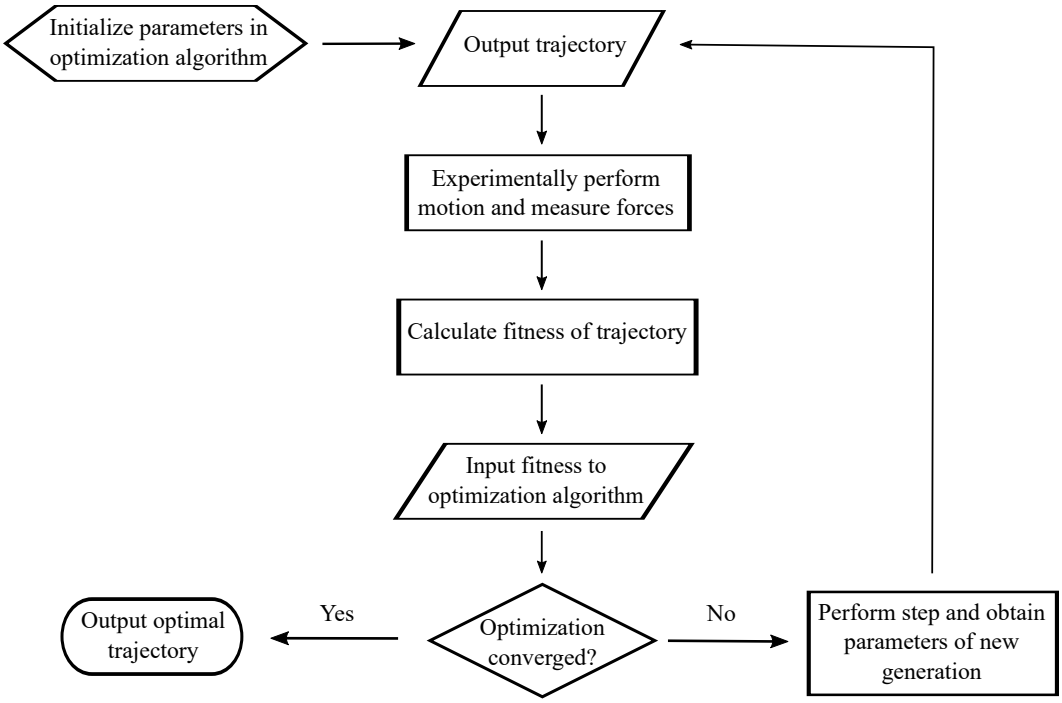

Figure 6.1: Flow chart of optimization process

(Kato and Liu, 2003; Martin and Gharib, 2018; Milano and Gharib, 2005). This experimental assessment is the approach employed in this work, which utilizes the experimental setup developed by Martin and Gharib (2018).

The optimization procedure is described in figure 6.1. Fin trajectories are parametrized employing several variables, including those presented in figure 6.2. Once the optimization algorithm is initialized, it outputs a trajectory whose fitness, as defined in equation 6.2, needs to be assessed. The trajectory is performed utilizing the experimental setup illustrated in figure 6.3 and the forces generated are measured. The fitness is then computed using this data and fed back to the optimization algorithm. If the optimization has converged, the optimal trajectory is output. If it has not converged, the algorithm performs a step in the optimization and outputs a new trajectory whose fitness needs to be assessed. The process is then repeated until and optimum is obtained.

The optimization method selected to perform this procedure is the covariance matrix adaptation evolution strategy (CMAES), which belongs to the broader category of evolution strategies. It is a stochastic method for black-box optimization capable of handling complex non-convex, non-smooth, noisy problems (Hansen, 2006; Hansen and Ostermeier, 2001). Evolution strategies have been successfully em-

ployed in many scenarios, including the optimization of fin properties and trajectory of De Margerie et al. (2007); Milano and Gharib (2005); Plucinski et al. (2007) and Clark et al. (2012).

Fin kinematics

The family of trajectories considered is periodic and can be parametrized with the use of ten different variables inspired by the motion of fish fins and insect wings. Their full mathematical description can be found in Martin and Gharib (2018) and Martin (2018). Figure 6.2a illustrates a multiview projection of the three dimensional motion of the fin, with the top portion illustrating the view from the back of the AUV and the bottom portion illustrating the top view. The edge of the fin is highlighted in black, with its center marked with a circle. The trajectory followed by this center point is shown as a black dashed line. To improve the visibility of the figures, the trajectories will be represented throughout this text as the two-dimensional projection, viewed from the back of the AUV, of the path followed by this centerpoint and the position of this highlighted edge. Two such diagrams can be viewed in figures 6.2b and c. The three-dimensionality of these trajectories, evident in the bottom portion of figure 6.2a, should, however, not be overlooked.

Figures 6.2b and c present some of the trajectory's defining parameters. Trajectories can be classified in two main types: figure-eight (figure 6.2b) or ellipse (figure6.2c). The stroke amplitude, ϕ, represents the maximum angular amplitude of motion of the centerpoint. The deviation angle, ψ, characterizes the thickness of its trajectory. The rotation angle determines the rotation of the wing along its z axis, as defined in figure 6.3b. The phase between this rotation and the motion of the centerpoint can also be modified, and is represented by β. The rotation does not necessarily occur at a constant rate, but can be accelerated at the edges of the trajectory. This acceleration is quantified by the rotation acceleration, K_v, that is a measure of the squareness of the rotation signal . The velocity of the centerpoint of the fin can be increased in certain sections of its trajectory, as represented in figure 6.2c. The section to be accelerated is specified by the speed-up code, S, while the speed-up value determines the relative speed of this section with respect to the remaining ones. The camber, λ, represents the asymmetry of the trajectory. Trajectories can, additionally, be performed at varying frequencies, f. The maximum and minimum values for each variable are presented in table 6.1, together with their convergence criteria. The limits on the variables are set according to the physical limitations of the experimental setup.

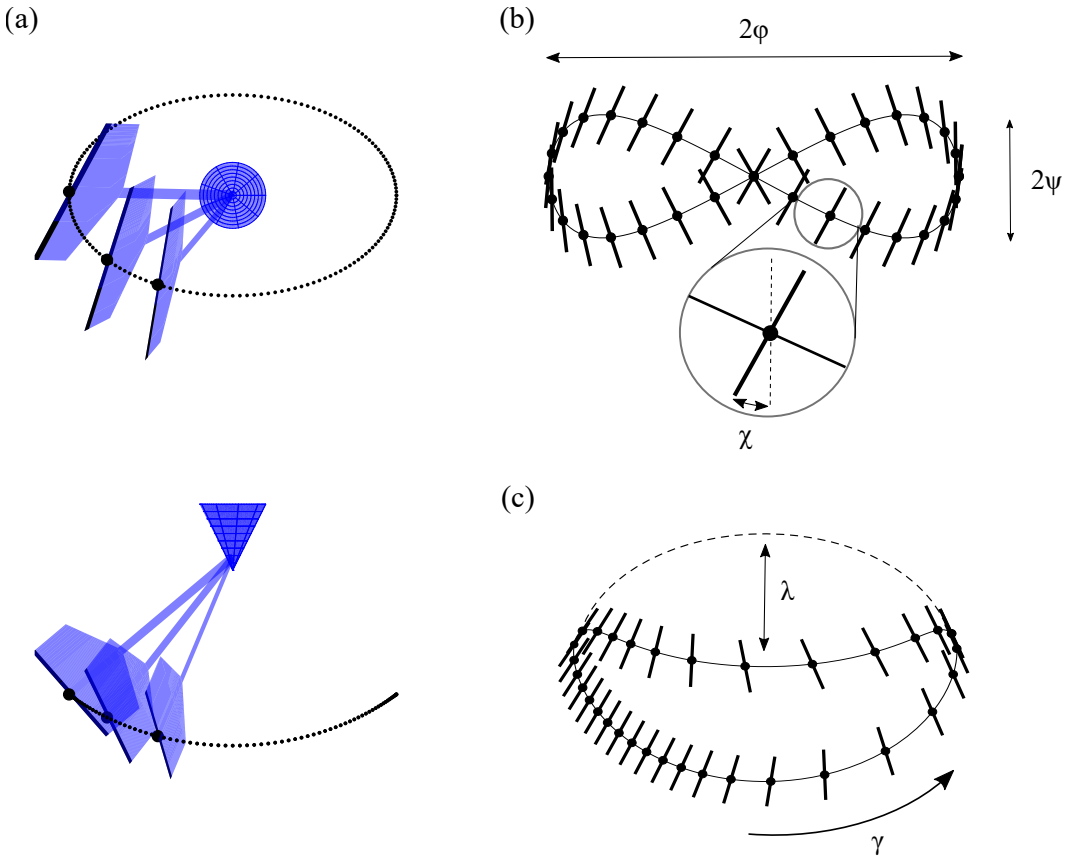

Figure 6.2: Description of fin kinematics. (a) Three-dimensional representation of the fin's motion. Back view is on top and top view is on bottom. The edge of the fin and its centerpoint are marked in black. The trajectory of the centerpoint is represented by a dashed line. The projection of the edge, centerpoint and its trajectory are used for the two-dimensional representations. (b) Definition of Stroke angle, ϕ, deviation angle, ψ, and rotation angle, χ. (c) Definition of camber, λ, and speed-up, γ.

Fitness

The objective of the optimization procedure is to obtain the best trajectory that generates a specified maneuvering force, which has been considered here to be a side force, i.e., a force in the x'-y' plane as defined in figure 6.3a, with x'-y'-z' being the laboratory reference frame. The target value of the force has been set to

$$F_{target} = 17mN$$

which is attainable with the fin geometry and experimental setup employed (Martin and Gharib, 2018). The variable to be minimized is therefore

Parameter	Symbol	Min. value	Max. value	Conv. criterion
Type	—	Figure-eight	Ellipse	Same type
Stroke angle	ϕ	20°	40°	3°
Deviation angle	ψ	0°	20°	3°
Rotation angle	χ	−70°	70°	3°
Rotation phase	β	0	2π	0.4
Rotation acceleration	K_v	0	1	0.2
Speed-up code	S	0	4	1
Speed-up value	γ	1	1.3	0.1
Camber	λ	0	1	0.2
Frequency	f	0.15 Hz	0.2 Hz	0.01 Hz

Table 6.1: Trajectory parameters, with corresponding range and convergence criteria.

$$w = \frac{|F - F_{target}|}{F_{target}}$$

The best trajectory has been defined as the trajectory which maximizes the efficiency

$$\eta = \frac{(\bar{F}_{x'}^2 + \bar{F}_{y'}^2)^{1/2}}{\overline{|F_x|}} \tag{6.1}$$

where x' and y' correspond to the laboratory reference frame and x to the wing reference frame (figure 6.3). This is a geometrical efficiency and represents the proportion of the normal forces generated by the fin that are oriented in the desired direction. It does not make any considerations with respect to the power necessary to generate the trajectory or output by the motion. Because maneuvering only occurs for small time intervals in comparison with cruising and the motion of the vehicle should be fast and well defined at those instants, it is more critical for the system to be able to perform motions in the desired direction exclusively than to do so utilizing little power. The defined efficiency responds to that need. These two objectives (closeness to target force and maximum efficiency) are combined to generate a fitness function given by

$$fit = 0.8\, w + 0.2\, |1 - \eta| \tag{6.2}$$

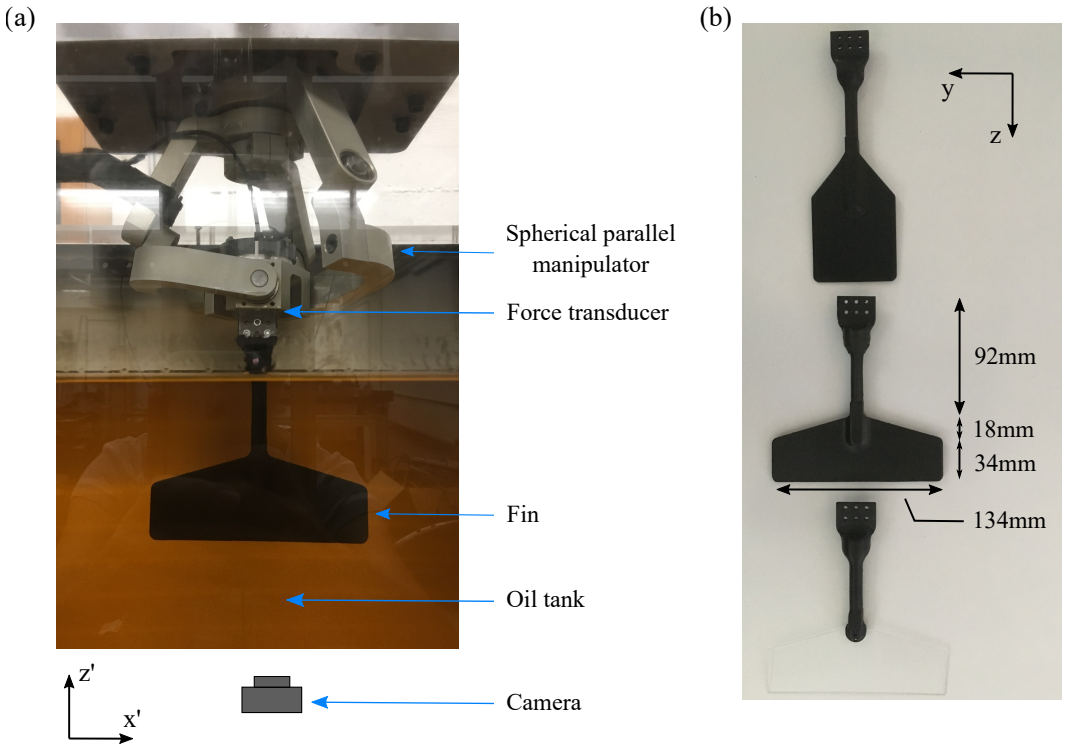

Figure 6.3: (a) Experimental setup, with laboratory frame axis (b) Fins tested with fin reference frame axis. From top to bottom AR=1, AR=4 (rigid) and AR=4 (flexible).

The value of this fitness is to be minimized in the optimization. Because it is more imperative for the force to approach the specified value than to do so efficiently, the proximity to the target force has been weighted more heavily in the fitness function. Martin and Gharib (2018) performed a sensitivity study that considered small variation in the weighting of both components, and concluded that these variations did not significantly impact the optimal trajectory obtained.

Experimental setup

A photograph of the experimental setup can be viewed in figure 6.3a. The motions are performed by a spherical parallel manipulator (SPM), which is an actuated spherical joint that can perform any three-dimensional rotation within a 50° cone (Sudki et al., 2013). The manipulator is set over an oil tank of dimensions 41cm × 50cm × 150cm. The oil (Chevron Superla White Oil #5) has a density of ρ = 835kg/m^3 and a viscosity of $\nu = 1.6\times10^{-5}$m^{2}s^{-1}. The resulting Reynolds numbers, based on the fin length, L_{fin}m and average tip velocity, U_{tip}, vary between $Re = L_{fin}U_{tip}/\nu$=270 – 900. The dimensions of the fins tested are presented in figure

6.3. The top fin was employed in the study of Martin and Gharib (2018) and has an aspect ratio of AR=1. The middle (rigid) and bottom (flexible) fins are employed in the current study and correspond to an aspect ratio of AR=4. All three fins have an equal surface area to allow for a direct comparison. The rigid portion of the fins (black) is 3D printed and the flexible portion (transparent) is cut from polycarbonate plates of density $\rho_s = 1200\text{kg/m}^3$, Young's modulus $E = 2.41\text{GPa}$ and Poisson ratio $\nu = 0.38$ and varying thickness.

The forces exerted on the plate are measured using a six-axis force transducer (ATI Nano17) located at the center of rotation of the system. They are sampled at 250 Hz and the weight of the fin, taking buoyancy into account, is subtracted from the data in post-processing. Three trials, consisting of at least ten cycles each, are performed for each trajectory. The first three cycles are eliminated to avoid the analysis of initial transients. The data is then averaged to obtain the mean forces at each instant of a single cycle.

Qualitative flow visualization was performed using small air bubbles, which are particularly suited for vortex observation because they are driven into their low-pressure core. The camera is placed below the oil tank (figure 6.3a) and the bubbles are allowed to rise until those with smallest diameter reach the bottom of the fin, at which time the images are acquired. A halogen light, shined through a small slit, was employed to illuminate the tank. This results in a higher illumination at the fin height, but bubbles at multiple heights are visible. The resulting images therefore contain information for different planes, allowing to visualize the three-dimensional structures but impeding quantitative two-dimensional measurements.